The response of a simulated mesoscale convective system to increased aerosol pollution: Part II: Derecho characteristics and intensity in response to increased pollution.

Michal Clavner[1], Lewis D. Grasso[2], William R. Cotton[1] and Susan C. van den Heever[1]

[1]Department of Atmospheric Science, Colorado State University, Fort Collins, Colorado, USA

[2]Cooperative Institute for Research in the Atmosphere, Colorado State University

Keywords: MCS, straight-line winds, derecho, pollution aerosols

Abstract

Mesoscale Convective Systems (MCS) are important contributors to rainfall as well as producers of severe weather such as hail, tornados, and straight-line wind events known as derechos. In this study, different aerosol concentrations and their effects on a derecho event are examined by simulating a case study, the 8 May 2009 "Super-Derecho", using the Regional Atmospheric Modeling System (RAMS), a cloud-resolving model with sophisticated aerosol and cloud microphysics. Three simulations were conducted that differed in the initial aerosol concentrations, spatial distribution and chemical composition as derived from output of GEOS-Chem, a 3D chemical transport model. In order to understand the impact of changes in aerosol concentrations on the derecho characteristics, the dynamical processes that produced the strong surface wind were determined by performing back-trajectory analysis during two periods of the simulated storm: the development and the onset of dissipation. A time dependent and non-monotonic trend was found between the intensity of the derecho and the increased aerosol concentrations that served as cloud condensation nuclei. During the formation period of the MCS, the non-monotonic trend was attributed to the microphysical impact of aerosol loading on the intensity of the cold pool; that is, the impact of aerosols on both the melting and evaporation rates of hydrometeors. The subsequent intensity changes within the cold pool modified the balance between the horizontal vorticity generated by the cold pool and that of the environment, thereby impacting the orientation of the convective updraft at the leading line. This, in turn, altered the primary flow that contributed to the formation of the derecho-strength surface winds. The simulation with no anthropogenic aerosols exhibited the strongest cold pool and the primary flow was associated with a descending rear inflow jet that produced the derecho winds over a larger region. The simulation with the highest amount of anthropogenic aerosols featured a

47 stronger mesovortex and the derecho winds were primarily due to stronger convective
48 downbursts. As the simulated storm matured, the changes in the derecho winds were found to be
49 associated with the strength of the mesovortex at the gust front. During the period when the
50 simulated storm began to dissipate, the non-monotonic trend in derecho intensity was associated
51 with a non-monotonic response in mesovortex strength to increased aerosol concentrations. A
52 moderate increase in aerosol concentrations led to the formation of a weaker mesovortex while a
53 greater increase in aerosol concentration led to the formation of a stronger mesovortex. The
54 formation of a stronger mesovortex was found to increase the contribution of the derecho winds
55 following a convective downburst associated with an "up-down" downdraft trajectory.

1. Introduction

In the High Plains of the United States, Mesoscale Convective Systems (MCS) can produce potentially damaging straight line winds over a large region. The meteorological phenomenon of straight line winds was discovered by Gustavus Hinrichs in 1888, who named the phenomena "derecho", a Spanish word which can be interpreted as "straight ahead". Johns and Hirt (1987) reintroduced the term “derecho” to describe convectively induced severe wind as "any family of downburst clusters produced by an extratropical mesoscale convective weather system". Based on operational forecasting experience and the definition of a family of downburst clusters (Fujita and Wakimoto, 1981; Johns, 1982), Johns and Hirt (1987) set the criteria for a severe wind event to be classified as a derecho based on the following spatial, temporal, and wind speed constraints:

- Concentrated area of reports consisting of convectively induced wind damage and/or convective gusts $\geq$26 ms^{-1} (50 knots). This area must have a major axis length of at least 400 km. The severe wind events must be caused by the same MCS and show a pattern of chronological progression.
- Within the derecho area there must be at least three severe wind reports separated by 64 km or more of either 18 -33 ms^{-1} and/or convective gusts of 33 ms^{-1} (65 knots) or greater.

In this paper derecho-strength (DS) winds will hereafter be referred to as DS winds. The criterion of "a pattern of chronological progression" refers to the following two types of derechos: progressive and serial. These two types are distinguished by the organization of an MCS, which produces the severe winds, as seen from radar reflectivity (Johns and Hirt, 1987). Radar signatures associated with downbursts and microbursts were identified and named "bow-echo" by Fujita (1978) due to the bowed appearance of the pattern of radar reflectivity. A bow-echo

79 pattern evolves as a convective downdraft reaches the surface and creates an enhanced outflow,
80 which subsequently propagates convective cells forward. Consequently, the apex of the bow
81 signifies the location of the greatest wind speeds near the surface (Fujita, 1978).

82 Two primary dynamical processes have been identified to explain the formation of the
83 surface outflow that constitutes a derecho. DS surface winds may result from (1) enhanced
84 downdrafts due to negatively buoyant air, which is in response to melting and evaporation of
85 precipitation (Fujita 1978), and/or (2) the transfer of high momentum air into the boundary layer
86 (Newton 1950) by a rear inflow jet (RIJ) (Smull and Houze, 1987). Convective features within
87 an MCS, such as supercell-like convective cells were found to intensify a derecho by
88 accelerating downdrafts that form due to the transport of negatively buoyant boundary layer air
89 within an "up-down" downdraft (Knupp, 1987; Bernardet and Cotton, 1998) and intensifying the
90 flow within a RIJ (Schmidt and Cotton, 1989). Another convective feature within an MCS that
91 was found to produce DS surface winds are meso-γ-scale (2-20 km) mesovortices (Orlanski,
92 1975; Wakimoto et al., 2006; Atkins and St. Laurent, 2009a). An open question centers on
93 potential dynamical changes in the above two processes in response to variations in
94 concentrations of aerosol serving as cloud concentration nuclei (CCN).

95 Past numerical and observational studies have found that increased aerosol concentrations
96 may lead to an invigoration of deep convective storms. Invigoration is due to the indirect effect
97 of aerosols serving as Cloud Condensation Nuceli (CCN) (e.g. Andreae et al., 2004; Khain et al.,
98 2005; van den Heever and Cotton, 2007; Lee et al., 2008; Rosenfeld et al., 2008; Fan et al., 2013;
99 Storer and van den Heever, 2013). These studies have shown that when higher aerosol
100 concentrations increase concentrations of CCN, smaller cloud droplets form leading to a
101 reduction in the collision-coalescence efficiency. As a result, warm rain production is reduced;

102 increased cloud droplet mass is transported vertically within an updraft, which then freezes
103 homogeneously and releases additional latent heat that subsequently intensifies the updraft.
104 Changes in aerosol concentrations have been found to impact both MCS precipitation and
105 intensity (e.g Khain et al., 2005; Tao et al., 2007; Li et al., 2009; Seigel and van den Heever,
106 2013; Lebo and Morrison, 2014; Saleeby et al. 2016) by altering the distribution and
107 characteristics of hydrometeors within an MCS, specifically the diameter of hydrometeors.
108 Changes in the diameter of hydrometeors directly impacts the potential for melting and/or
109 evaporation of hydrometeors (van den Heever and Cotton, 2004; Bryan and Morrison, 2012;
110 Adams-Selin et al., 2013; Storer and van den Heever, 2013) and, consequently, the intensity
111 of cold pools (van den Heever and Cotton, 2004; Tao et al., 2007; Li et al., 2009; Seigel et al.,
112 2013; Grant and van den Heever, 2015).

113 Variations in the intensity of a cold pool have been shown to alter other characteristics of
114 an MCS. Adams-Selin et al., (2013) discussed the sensitivity of the structure and intensity of a
115 simulated bow-echo to the intensity of a cold pools. Weisman (1992) showed the impact of cold
116 pool intensity on the convective structure associated with a derecho event, as well as the intensity
117 of a RIJ. Seigel and van den Heever, 2013 found that changes in hail size may introduce a
118 positive feedback on RIJ intensity within a squall line via the recirculation of hydrometeors
119 between the convective and stratiform regions. Cold pool intensity was also found to impact
120 baroclinically generated horizontal vorticity within a cold pool, thereby impacting the balance
121 between horizontal vorticity within a cold pool and that of the low-level (0-3km) environmental
122 wind shear at the leading line of an MCS: a central concept in RKW-theory (Rotunno et al.,
123 1988). Changes in the balance between horizontal vorticity within a cold pool and the low-level
124 environment were found to impact the intensity of the RIJ by altering the tilt of convective cores

125 (Weisman, 1992, 1993) as well as the formation of mesovortices along an outflow boundary by
126 modifying the amount of horizontal vorticity tilted into the vertical (Weisman & Trapp 2003).
127 An implication of the above studies is that the sensitivity of a derecho event to changes in
128 aerosol concentrations will depend on the potential impacts that aerosols may have on the parent
129 MCS, particularly cold pool intensity. In addition, the response of MCS morphology to aerosol
130 impacts was also found to be dependent on characteristics of the environment such as humidity
131 (Khain et al., 2005; Tao et al., 2007) and vertical wind shear (Fan et al., 2013; Lebo and
132 Morrison, 2014). As a result, MCS behavior can change from one event to the next (e.g Tao et
133 al., 2007).

134 In this study, the impact of enhanced anthropogenic aerosols on the case study of 8 May
135 2009 "Super derecho" MCS is investigated. The derecho event of the 8 May 2009 storm has
136 been analyzed in several past studies which focused on the environmental characteristics of the
137 system (Coniglio et al., 2011, 2012; Keene and Schumacher, 2013). In addition, other studies
138 concentrated on the development of meso-β (2-200km) (Weisman et al., 2013; Evans et al.,
139 2014), and meso-γ (2-20km) vortices (Przybylinksi et al., 2010; Xu et al., 2015a, 2015b) in the 8
140 May 2009 MCS. This study adds to the current body of work by examining the impacts of
141 increased anthropogenic aerosol concentrations on the characteristics of this system. In part I
142 (Clavner et al., 2015; hereafter referred to as Part I), the impact of increasing aerosol
143 concentrations that can serve as CCN were found to lead to stronger updrafts, enhanced
144 convective precipitation, and a decrease in stratiform precipitation. This paper is organized as
145 follows: the 8 May 2009 case study is presented in section 2 while the model set up and aerosol
146 sensitivity tests are given in Section 3. The results of changing aerosol concentration on the

147 simulated 8 May 2009 derecho are presented in Section 4. A discussion and conclusions are
148 given in section 5 and 6, respectively.

149 **2. The 8 May 2009 MCS**

150 Several previous studies have examined many different aspects of the 8 May 2009 MCS.
151 In particular, this event has been characterized as a leading-line (Coniglio et al., 2011; Weisman
152 et al., 2013), trailing stratiform (Houze et al., 1989; Parker and Johnson, 2000) bow-echo (Fujita,
153 1978) MCS, which developed a warm-core meso-β-scale (20-200 km) vortex in its later stage
154 (Weisman et al., 2013; Evans et al., 2014), as well as several meso-γ-scale (2-20 km) vorticies
155 (Xu et al., 2015a, 2015b). The MCS developed in western Kansas at ~0600 UTC and moved
156 south-southeastwards to the southern Appalachians, traveling over a thousand miles before
157 dissipating at 1900 UTC (Coniglio et al., 2011; Storm Prediction Center (SPC)). Unique
158 environment characteristics that aided in the genesis and longevity of the 8 May 2009 MCS
159 included a strong Low Level Jet (LLJ) and anomalously large values of precipitable water (PW)
160 content along an east-west oriented surface boundary (Coniglio et al. 2011). A more detailed
161 description of the MCS environment, structure and propagation is found in Part I. DS winds that
162 were produced by the 8 May 2009 MCS occurred along the entire storm track, from western
163 Kansas to the region where the system dissipated, west of the Appalachians (Fig. 1). As the
164 storm moved from Kansas into Missouri, a large scale bow-echo developed and several cyclonic
165 meso-γ vortices formed near the apex of the bow-echo on the low-level convergence zone
166 (Pryzybylinksi et al., 2010). Analysis of reflectivity and Doppler velocity over southwest
167 Missouri showed that the meso-γ vortices occurred simultaneously at ~1330 UTC and that the
168 strongest meso-γ vortex formed in the region where the cold pool and low level shear were

169 balanced, resulting in vertically-erect towers (Przybylinksi et al., 2010). The evolution of the
170 meso-γ vortices within the 8 May 2009 MCS was examined numerically by Xu et al. (2015a;
171 2015b) and were found to form at the leading line of the bow-echo, similar to the observational
172 findings of Pryzybylinksi et al. (2010).

173 As the storm matured, the northern end of the bow echo occluded forming a warm core
174 meso-β vortex (Weisman et al. 2013; Evan et al. 2014) that was apparent in radar imagery as a
175 comma shape echo (see Fig. 1f, Part I). During the evolution of the meso-β vortex (~1700
176 UTC), the cold pool associated with the MCS weakened. As a result, strong surface winds
177 developed in response to the deepening and intensification of the meso-β vortex to the surface
178 rather than the cold pool forcing (Weisman et al. 2013; Evan et al. 2014).

179 In summary, the 8 May 2009 MCS, DS winds were found to be generated due to
180 enhanced convective downdrafts, in association with the storm generated cold pool and a
181 descending RIJ. Furthermore, strong surface winds were found to be enhanced due to the
182 formation of meso-γ vortices along the gust front and in association with a warm core meso-β
183 vortex that formed during the later stages of the 8 May 2009 MCS. These past studies show that
184 there are several different dynamical processes that may be responsible for the formation of DS
185 surface winds. The impact of changes in aerosol concentration on these processes is the focus of
186 this study.

187 **3. Numerical Model and Experiment Setup**

188 3.1 Model Configuration

189 The 8 May 2009 MCS case study was simulated using the Colorado State University
190 Regional Atmospheric Modeling System (RAMS) version 6 (Cotton et al., 2003; Saleeby and

van den Heever, 2013). The RAMS model simulation was configured as a heterogeneous, cloud resolving mesoscale model with three interactive grids (see Fig. 4, Part I). Grids 1 and 2 were set up with a horizontal grid spacing of 40 and 8 km, respectively. The finest nested grid was set up with a horizontal grid spacing of 1.6 km and covers the entire region of the simulated MCS from genesis to decay. Detailed information on the RAMS model setup is described in section 3.4 of Part I.

3.2 RAMS simulations

In order to examine the impact of increased aerosol concentrations on the derecho characteristics of this simulated MCS, a set of three numerical simulations was performed: CLEAN, POLLUTED, and 5xPOLLUTED. As described in section 3.1, the three simulations utilized the same RAMS model configuration with the exception of their initial aerosol concentrations and spatial distribution. Aerosol concentrations were derived from GEOS-Chem (Bey et al., 2001), a 3D global chemistry model. Additional details about GEOS-Chem, output from GEOS-Chem, and the method of implementation of aerosols with RAMS are found in Part 1. Fig. 5 (Part I) presents the vertical profiles of the average total aerosol concentrations [cm^{-3}] at the time of genesis of the MCS (0630 UTC) in the three different RAMS simulations. The CLEAN and POLLUTED simulations were initialized with aerosols derived from only natural emissions (no anthropogenic sources), and both natural and anthropogenic emissions, respectively. The 5xPOLLUTED simulation was initialized with the same aerosol distribution as the POLLUTED simulation, except that both aerosol mass and concentrations were multiplied by a factor of five in order to examine the impacts of a highly polluted scenario.

212 3.3 Back Trajectory Analysis

213 In order to understand the impact of changes in aerosol concentrations on the derecho
214 characteristics, dynamical processes that produced the simulated DS winds were first
215 determined. Dynamical processes in this study were analyzed by computing back-trajectories
216 (BT) with a Lagrangian model (LM) (Grasso, 1996) from grid points with DS winds for all three
217 RAMS simulations. Grid points with DS winds were determined according to the surface wind
218 speeds at the second vertical model level above ground level (~75m AGL). Wind speed
219 magnitudes of at least 26 ms^{-1} were considered to be part of the simulated derecho event,
220 following the minimum wind speed criteria set by Johns and Hirt (1987).

221 For each of the three simulations, RAMS was rerun for 60 minutes for different periods
222 of the storm. During each 60 minute time period, the components (u, v, and w) of the 3D wind,
223 virtual potential temperature, and the total condensate mixing ratio were extracted from the
224 Eulerian RAMS Grid 3 at each time step (3.33 seconds). Values of the extracted variables were
225 then transferred, by a tri-linear spatial interpolation scheme within the LM to the parcel's
226 location. Advection of a parcel was accomplished with the use of the 4^{th} order Runge-Kutta
227 method and a time step of 3.33 seconds, corresponding to the output time of RAMS velocity
228 data: Interpolation in time was not needed.

229 The BTs were analyzed, along with various instantaneous fields extracted from RAMS every 30
230 minutes (output time interval of Grid 3 data for all three simulations) around the location of a
231 parcel including budget tracking of microphysical processes and cold pool characteristics. The
232 number of BT performed for each RAMS simulation depended on the number of grid points with
233 DS winds and varied from 50-300.

234 **4. Simulation Results**

235 In all three RAMS simulations, convective elements not directly associated with the MCS
236 also developed in Grid 3. In order to isolate the DS winds produced by the simulated 8 May 2009
237 case study, data from the other convective elements were numerically filtered out. The filtering
238 technique, described in detail in section 3.1 of Part I, incorporated parameters outputted every 30
239 minutes such as estimated cloud top temperature [C], precipitation rate [$mmhr^{-1}$] and vertically-
240 integrated total condensate [kgm^{-2}]. In this study, data analyzed from the RAMS simulated MCS
241 were taken from MCS genesis at 0630 UTC until 1730 UTC, after which the method for
242 isolating the MCS was less reliable due to the dissipation of the system and subsequent
243 fragmentation of the MCS' stratiform-anvil, as well as the close proximity of the storm to
244 neighboring convection.

245 In order to assess the simulated derecho event, a map of surface wind magnitudes during
246 the entire analysis period is presented in Fig. 2, for each of the three RAMS aerosol sensitivity
247 simulations: CLEAN (Fig. 2a), POLLUTED (Fig. 2b) and 5xPOLLUTED (Fig. 2c). Each figure
248 contains the maximum wind speed at each output time (30 minutes) during the analysis period
249 (0630-1730 UTC) superimposed on the same figure in order to represent a map of the simulated
250 derecho event as a function of space and time. All three of the simulations produced swaths of
251 DS surface winds along a corridor from west Kansas progressing south southeastwards through
252 southeast Kansas and the southern portion of Missouri. These cumulative maps compared
253 favorably with the locations of the SPC reports of wind speeds greater than 50 knots (26 ms^{-1})
254 (Fig. 1) during 8 May 2009. A detailed comparison of the simulated MCS's formation, location
255 and structure to observations is given in section 4.2 of Part 1.

256 Changes in the simulated derecho characteristics as a result of variations in aerosol
257 concentrations are now investigated. Two metrics are used to quantify the intensity of the
258 simulated derecho during the analysis period (0630 and 1730 UTC): the number of grid points
259 with DS wind and the magnitude of the DS wind speed (Johns and Hirt, 1987). A quantitative
260 comparison of these two metrics among the three RAMS simulations are presented in Fig. 3.
261 From the analysis of the number of grid points with DS winds over time, three stages within the
262 simulation are apparent: intensification, mature and dissipation. During the intensification stage
263 of the MCS, the area with DS wind was the largest and decreased with time as the storm matured
264 and began to dissipate. This suggests that within each of the simulations, different mechanisms
265 may be responsible for the generation of the DS winds as the MCS matured and weakened.
266 Unlike the changes in the number of grid points with DS winds (Fig. 3a), the mean DS wind
267 speed for both the CLEAN and 5xPOLLUTED simulations are similar throughout the analysis
268 period (Fig. 3b). Only the POLLUTED simulation shows a decrease in mean DS wind speeds as
269 a function of time. This is discussed in section 4.2.

270 The intensity of the DS winds was further investigated by calculating the normalized
271 distribution of the DS wind magnitudes during different periods of the storm: intensification
272 (0630-0930), mature (1000-1330 UTC) and dissipation (1400-1730 UTC). The normalized
273 distribution within three ranges of DS winds were examined corresponding to the DS minimum
274 threshold wind speed (26 ms^{-1}) and the stronger DS gusts (34 ms^{-1}) (Johns and Hirt, 1987) in
275 intervals of 4 ms^{-1} defined here as: weak (26-30ms^{-1}), moderate (30-34 ms^{-1}) and strong (34>ms^{-1}).
276 The bin count was normalized by the total number of grid points with DS winds within each
277 simulation for the three periods (Fig. 4). During the intensification stage of the MCS (Fig. 4a), a
278 monotonic trend is apparent where increasing aerosol concentrations lead to stronger DS winds

(Fig. 4a) over a smaller area (Fig. 3a). The increase in DS wind strength is evident through the decrease in the percentage of grid points within the weak DS wind category and an increase in the strong DS category (Fig. 4a). That is, the percentage of grid points in the weak bin decreases from the CLEAN (49%), POLLUTED (~47 %) to the 5xPOLLUTED case (42 %). However, in the strong bin, the percentage of grid points increases from the CLEAN (31 %), POLLUTED (33 %) to the 5xPOLLUTED case (37 %).

During the mature stage (Fig. 4b) the intensity of the DS winds slightly decreases for the POLLUTED simulation, as seen by a higher bin count within the weak category, however, this decrease is even more prevalent within the dissipation stage (Fig. 4c). Within the POLLUTED simulation both the area of DS winds and the strength of DS winds decrease with time (Fig .3b and Fig. 4c). Therefore, within the dissipation stage, an increase in aerosol concentration led to a non-monotonic trend in the derecho intensity since only the moderate increase in aerosol concentrations was found to weaken the derecho. The percentage of grid points in the weak bin for the POLLUTED (64%) simulation was the highest in comparison to the CLEAN (55%) and 5xPOLLUTED case (52 %) and the lowest (8%) within the strong bin in comparison to 27% and 26% for the CLEAN and 5xPOLLUTED, respectively.

Among the three simulations, the differences between both area and intensity occurred primarily within both the intensification (Figs. 3a and 4a) and dissipation time periods (Figs. 3b and 4c). As a result, additional analysis were performed by conducting a 60 minutes BT analysis for the three simulations, during these times. BT analysis facilitates a time continuous examination on a finer time scale, in comparison to the instantaneous snapshots every model output time, of the air flow that generates the DS winds at the surface during these time periods. Thereby an examination of this flow among the three simulations permitted a detailed diagnosis

of the dynamics responsible for generation of the DS winds within each simulation and the impacts of changes in aerosol concentrations on the flow. Findings of the derecho characteristics and results from BT analysis are presented in the following sections.

4.1. Simulated Derecho at 0900 UTC: Intensification Stage

During this time, the dominant region with DS winds occurred in all three simulations within the upstream region of the convective line in association with a Cell Bow Echo (Klimowski et al., 2004) that was embedded within the bowed convective line. Cell Bow Echoes are described as strong thunderstorms on the scale of 10-25 km which have bowed out due to strong outflow (Klimowski et al., 2004). The region with DS winds (boxed area in Fig. 5) is at the gust front portion of the Cell Bow Echoes. Fig. 6 presents the density potential temperature within the boxed are in Fig. 5. The relative difference between the cold pool density potential temperature (Emanuel, 1994) and that of the environment is a measure of cold pool buoyancy (Tompkins 2001; Seigel et al. 2013). It is also a useful indication of the location of the gust front of the storm (Charba, 1974). Fig. 6 also shows area with DS winds (contoured in red), and the initialization location of the back-trajectory (BT) parcel locations within the three RAMS simulations: CLEAN, POLLUTED and 5xPOLLUTED.

The BT flow is presented in Fig. 6c, Fig7c and Fig 8c for the CLEAN, POLLUTED and 5xPOLLUTED simulations as a function of location, as well as the parcels' horizontal velocity along its trajectory. The BT airflow shows that the DS winds originated from two main upper-level flows: a descending RIJ and an up-down downdraft (UDD). The importance of these two flows in the generation of the strong surface winds differs among the simulations, as determined by the fraction of the BT that followed each of the two flows. The dominant BT airflow in the CLEAN simulation was the RIJ (Fig. 6c), which accelerated towards the leading convective line

325 at higher elevations (~3000m AGL) than the RIJ in the POLLUTED (Fig. 7c) and
326 5xPOLLUTED (Fig. 8c) simulations. In the 5xPOLLUTED simulation (Fig. 8c), the dominant
327 flow consisted of an UDD. The UDD air originated near the surface east (upstream) of the storm,
328 slowly ascended with weak vertical velocities (~4-7 ms^{-1}) (not shown) toward the leading
329 convective cell, turning cyclonically and then rapidly descending (Fig. 9c) as the parcels
330 encounter the precipitating downdraft on the upstream side of the convective updraft (Fig. 8c).
331 The cyclonic turn of the parcels as they entered the leading convective line is explained by the
332 meso-γ vortex (contoured in green, Fig. 8c), indicated by a volume of relative vertical vorticity
333 greater than $0.01s^{-1}$ (Weisman and Trapp, 2003). A third flow in addition to the RIJ and UDD
334 flow is also apparent in the 5xPOLLUTED simulation. This flow originated at 4 km AGL from
335 the south-south west and is similar to the midlevel downdraft branch described in Knupp (1987).
336 Within the POLLUTED simulation (Fig. 7c), BT flow indicates that both the RIJ and the UDD
337 contributed in the formation of the DS winds.

338 A comparison of all the BT flows during the parcel's descent to the surface, for all three
339 simulations is presented in Fig. 9 and compares the mean downdraft speed, horizontal speed,
340 total condensate mixing, and virtual potential temperature. Fig. 9 shows that increasing the
341 aerosol number concentration leads to a shift in the dominant BT flow from a prevalent RIJ in
342 the CLEAN simulation, categorized by the stronger horizontal velocities at higher levels (Fig.
343 9d) to a dominant UDD flow within the 5xPOLLUTED simulation, defined by stronger
344 downdraft speeds (Fig. 9c) which reach downburst intensities of greater than $-10ms^{-1}$ (Fujita,
345 1978). The shift in the BT flow from the RIJ to the UDD with increased aerosol pollution is
346 explained by the response of the convection orientation at the gust front to aerosol-induced
347 changes in the cold pool characteristics produced by the storm, following the RKW theory

348 (Rotunno et al., 1988). A stronger RIJ forms when the main convective updraft is tilted upshear,
349 forming a horizontal vorticity gradient between that of the cold pool and the tilted updraft
350 (Weisman, 1992), as seen for the CLEAN simulation (Fig. 6b). A stronger meso-γ vortex will
351 develop when the horizontal vorticity generated by the cold pool is in balance with that of the
352 environmental shear (Atkins and St. Laurent, 2009b), leading to a more upright updraft, as seen
353 in the 5xPOLLUTED simulation (Fig. 8b). Such a balanced state promotes the generation of
354 relative vertical vorticity by the tilting of horizontal vorticity into the vertical as well as by
355 stretching of the vortex tube (Atkins and St. Laurent, 2009b).

356 An increase in aerosol number concentration led to a non-monotonic trend within the
357 cold pool temperature, indicated in the BT virtual potential temperature (Fig. 9f) as well as the
358 surface plots of the density potential temperature (Fig. 6a, 7a and 8a). Changes in aerosol
359 number concentrations were found to alter the strength of the cold pool (both temperature and
360 depth) due to the changes they induce in the precipitating hydrometeor characteristics. In part I,
361 we found that at this time, higher aerosol number concentrations enhanced both cold and warm
362 rain formation in the 5xPOLLUTED simulation and warm rain formation in the POLLUTED
363 simulation, leading to higher precipitation rates and the formation of larger raindrops near the
364 surface in both cases. Within the CLEAN simulation the precipitation rates as well as rain
365 droplets diameters were found to be smaller in comparison to both the POLLUTED and
366 5xPOLLUTED simulations. Therefore, aerosol-induced changes in precipitation formation
367 mechanisms impacted both the rates of evaporation and melting of the hydrometeors, which in
368 turn, altered the cold pool strength.

369 Here the changes in precipitation and evaporation are seen by examining the mean total
370 condensation mixing ratio (Fig. 9e) and mean virtual potential temperature (Fig. 9f) during the

371 decent of the parcels to the surface. Fig. 9e indicates that below 1 km, condensate loss due to
372 evaporation occurred in all three of the simulations, however, at different altitudes and with
373 different magnitudes. In the CLEAN simulation, evaporation is most evident near the surface,
374 while for the 5xPOLLUTED simulation, evaporation occurs throughout the entire 1km AGL
375 depth. In the POLLUTED simulation, the near constant value of mean condensate mixing ratio
376 indicates that at this time, this simulation exhibited the least amount of evaporation, and
377 therefore, least amount of cooling within the downdraft in comparison to CLEAN and
378 5xPOLLUTED. Due to the enhanced precipitation formation in the 5xPOLLUTED simulation,
379 more mass was available to be evaporated at lower levels. However, the smaller raindrops (Part
380 1, Fig. 14a) within the CLEAN simulation increased the evaporation rates. The downdrafts were
381 the warmest in the POLLUTED simulation (Fig. 9f) due to a decrease in evaporation, as seen in
382 the near constant value of mean total condensate below 1 km AGL (Fig. 9e), indicating smaller
383 amounts of total condensate loss within the downdraft in comparison to both CLEAN and
384 5xPOLLUTED (Fig. 9e). This decrease in evaporation is explained by both larger raindrops as
385 well as smaller rain rates in the POLLUTED case in comparison to the 5xPOLLUTED
386 simulation. Within the CLEAN simulation, the higher evaporation rates, in comparison to both
387 the simulations with higher aerosol concentrations, impacted the cold pool strength by
388 decreasing its density potential temperature and thus, increasing the horizontal gradient in
389 density potential temperature between the cold pool and the environment and hence it's negative
390 buoyancy and strength (Tompkins, 2001).

391 The orientation of the convection at the leading line shows that in the CLEAN
392 simulation, for which the cold pool is the strongest, the updraft is tilted upshear which results in
393 the BTs being predominantly from the RIJ (Fig. 6b). For the 5xPOLLUTED simulation, the cold

394 pool is slightly weaker in comparison to the CLEAN simulation, leading to a more upright
395 convective updraft (Fig. 8b), which enhanced the intensity of the meso-γ vortex. In the
396 POLLUTED simulation, the cold pool was the weakest of the three simulations at 0900 UTC,
397 and the convection at the leading line is seen to be tilted downshear. This limited the amount of
398 vertical vorticity generated by stretching and produces a weaker meso-γ vortex (Fig. 7b).
399 Despite the weaker cold pool and the shallower meso-γ vortex in the POLLUTED simulation,
400 the downdraft speeds within the UDD were comparable to that of the 5xPOLLUTED simulation,
401 emphasizing that the accelerations contributing to the stronger downdrafts in the former occurred
402 at levels below 2 km AGL, consistent with the characteristics of an UDD (Knupp, 1987). The
403 shift of the BT flow from a RIJ (CLEAN) to a UDD associated with the meso-γ vortex
404 (5xPOLLUTED) explains why DS winds were stronger and occurred over a smaller region at
405 0900 UTC for the more polluted simulations.

406 4.2. Simulated Derecho at 1500 UTC: Dissipation Stage

407 At 1500 UTC the region with DS surface winds encompassed the smallest area relative to
408 the entire analysis period (Fig. 3a) for both the CLEAN and POLLUTED simulations. After
409 1400 UTC, the convective region of the MCS began to diminish and the storm became
410 dominated by stratiform precipitation (Fig. 9 and 11, Part I), indicating the onset of MCS
411 dissipation. During the intensification stage of the storm, an increase in aerosol number
412 concentrations introduced a monotonic response in the derecho characteristics where the increase
413 in aerosol concentrations produced stronger DS winds over a smaller region in comparison to the
414 CLEAN simulation. In contrast, at 1500 UTC, the increase in aerosol number concentrations led
415 to a non-monotonic response in both DS strength and area. Relative to the CLEAN simulation, a
416 moderate increase in aerosol concentration (POLLUTED) decreased the DS wind area by 36%

417 (Fig. 3a) as well as the magnitude of the DS winds (Fig. 3b and 4c), while a greater increase in
418 aerosol concentration (5xPOLLUTED) produced DS winds over an area 200% larger (Fig. 3a)
419 with similar DS wind intensity (Fig. 3b and 4c). The location of the DS winds at 1500 UTC for
420 all three cases are superimposed on the surface density potential temperature in Fig. 10, which is
421 representative of the location of the cold pool and hence the gust front. At this time, all three
422 simulations produced DS winds in close proximity to a meso-γ vortex (outlined in green contours
423 of relative vertical vorticity in Fig. 10) at the leading edge of the gust front. The location of a
424 meso-γ vortex at the gust front in this study is supported by observations (Weisman and Trapp,
425 2003), observations for the 8 May 2009 MCS in particular (Przybylinksi et al., 2010), and a
426 recent numerical simulation of the MCS (Xu et al., 2015b). For both the CLEAN (Fig. 11a) and
427 5xPOLLUTED (Fig. 11c) simulations, two BT flows are apparent: the RIJ and the UDD, while
428 the BT flow only follows a RIJ for the POLLUTED simulation (Fig 11b). Comparisons of the
429 characteristics of the RIJ in the three simulations are shown in Fig. 12. The RIJ was similar in
430 both the intensity and elevation in the CLEAN and POLLUTED simulations. Therefore, the
431 smaller area with DS winds, as well as the weaker DS winds, in the POLLUTED simulation,
432 appears to be explained by the lack of an UDD within this simulation.

433 As seen in section 4.1, the intensity of a meso-γ vortex impacts the UDD. Therefore, in
434 order to understand why the POLLUTED simulation did not form a UDD flow regime, the
435 intensity of the meso-γ vortex was compared among the simulations. This was done by
436 examining the maximum vertical relative vorticity within the meso-γ vortex (Fig. 13a), identified
437 as a 3D volume where values of relative vertical vorticity are at least $0.01 s^{-1}$, in keeping with
438 previous studies (e.g. Weisman and Trapp 2003). The maximum updraft velocity and minimum
439 perturbation Exner function were examined in Fig. 13b and 13c, respectfully. The column mean

of the maximum relative vertical vorticity was 0.02, 0.015 and 0.017 s^{-1} in the 5xPOLLUTED, POLLUTED and CLEAN simulations, respectively. Furthermore, the meso-γ vortex in the 5xPOLLUTED simulation was 3 km deeper in comparison to both CLEAN and POLLUTED. Therefore, the strongest meso-γ vortex (Fig. 13a) occurred in the 5xPOLLUTED simulation, followed by the CLEAN, and the weakest meso-γ vortex occurred in the POLLUTED simulation. The weaker meso-γ vortex within the POLLUTED simulation did not result in the development of an UDD and this flow regime could not contribute to the DS winds at the surface. In order to fully understand how changes in aerosol concentrations led to the non-monotonic trend in the development of the meso-γ vortices, vorticity budget analyses needs to be conducted. This is left for future work.

The UDD flow characteristics between the CLEAN and 5xPOLLUTED simulations is further examined by comparing the horizontal wind speeds of the parcels as they descended to the surface following the UDD (Fig. 14). In the 5xPOLLUTED simulation the parcels entered the meso-γ vortex with a higher horizontal velocity (Fig. 14b). Therefore, the higher horizontal velocities of the parcels at higher altitudes led to the formation of DS winds at the surface indicating that the transfer of horizontal momentum from higher levels contributed to the formation of the DS winds. In contrast, in the CLEAN simulation, parcels entered the meso-γ vortex at both lower altitudes and lower horizontal wind speeds (Fig. 14a). The parcels accelerated to DS winds only after descending to the surface. The near surface acceleration within the CLEAN simulation is explained by higher evaporation rates, which is seen by the lower density potential temperatures (Fig. 10). As was shown in part I, the 5xPOLLUTED simulation produced larger rain droplets at this time. These droplets evaporated less readily thereby enhancing the amount of precipitation reaching the surface and decreasing the

463 evaporation potential. The horizontal acceleration of the UDD at higher levels within the
464 5xPOLLUTED simulation is explained by a larger horizontal pressure gradient force induced by
465 the lower pressure within the stronger meso-γ vortex (Fig. 13c).

466 **5. Discussion**

467 The sensitivity of the 8 May 2009 derecho to aerosol loading has been investigated by
468 numerically simulated the storm and conducting three simulation in which aerosol number
469 concentrations differed. Due to the complex nature of the dynamics of an MCS, identifying the
470 impact of increased aerosols on the strength of the near surface convective outflow is
471 challenging. This is because aerosols serving as CCN were found in this study to modify the
472 strength of a derecho in the following three ways: (1) directly modifying the intensity of the
473 downdrafts due to phase changes of hydrometeors; (2) indirectly modifying the relationship
474 between the horizontal vorticity generated in association with the environmental shear and that
475 baroclinically-generated by the storm-produced cold pool; and (3) modification of the strength of
476 the mesovortex due to changes in vertical relative vorticity.

477 Previous numerical studies have shown that mesoscale storm dynamics and longevity are
478 sensitive to changes in hydrometeor diameters through changes to the melting and evaporation
479 rates, and thus, the strength of the storm-produced cold pool. van den Heever and Cotton (2004)
480 found that decreasing hail diameter sizes increased cold pool strength due to an increase in
481 melting and subsequent evaporation. Smaller hail hydrometeors increase the melting potential
482 due to smaller terminal fall speeds and an increase in the integrated surface area exposed to
483 melting. Similarly, Adams-Selin et al. (2013) found cold pool intensity to vary as a function of
484 graupel size and density. Both studies demonstrated that smaller ice hydrometeors led to stronger

485 cold pools. In Part I of this study, increases in aerosol concentration were found to produce larger
486 rain drops and hail stones which contributed to an enhancement in the amount of convective
487 precipitation produced by the storm. The smaller rain and hail diameters within the CLEAN
488 simulation produces the stronger cold pools found in Part II of this study. However, the strength
489 of the cold pool was found to be sensitive to both the size of the precipitating hydrometers as
490 well as precipitation rates. During the intensification stage of the MCS, the strongest cold pool
491 was found in the CLEAN simulation followed by the 5xPOLLUTED simulation, and the weakest
492 cold pool evident in the POLLUTED simulation. This was attributed to higher rain rates in the
493 5xPOLLUTED simulation which yielded more hydrometeor mass available to be melted and
494 evaporated. During the dissipation stage of the MCS, when the differences in the convective rain
495 rates were smaller among the simulations, a monotonic trend was found where increased aerosol
496 concentrations formed weaker cold pools due to the larger precipitating hydrometers. The
497 changes in cold pool strength modify the formation of Derecho-Strength (DS) winds at the
498 surface by impacting the formation of the RIJ (Weisman 1992), as well as the strength of meso-γ
499 vortices at the gust front (Atkins and St. Laurent, 2009b).

500 In order to understand the impact of aerosol loading on the simulated derecho in this case
501 study, back trajectory analysis from the locations with DS winds at the surface were performed
502 for all three of the simulations during two stages of the simulated MCS: intensification and
503 dissipation. Results of the BT analysis suggested that two types of air flows contributed to the
504 formation of the DS winds: (1) a rear inflow jet (RIJ) and (2) downdrafts following an up-down
505 downdraft (UDD) trajectory associated with a meso-γ vortex. The findings that the DS winds
506 were generated by both a RIJ and flow associated with a meso-γ vortex is consistent with the
507 findings of Atkins and St. Laurent (2009b). Furthermore, the findings of air parcels

508 "originating" within the boundary layer contribution to the formation of DS following a
509 trajectory of an UDD is consistent with previous findings (Knupp, 1987; Bernardet and Cotton,
510 1998). A schematic summarizing the 3D flow driving the DS winds within the simulated 8 May
511 2009 derecho event is presented in Fig. 15 derived from the back-trajectory analysis conducted
512 in this study . The flow following the UDD reaches the surface south of the meso-γ vortex,
513 similar to the findings of Atkins and St. Laurent (2009b). It is important to note that the RIJ
514 captured in the 60 minute back trajectory flow is focused near (~50 km) **of**the convective
515 line and does not include the entire extent of the RIJ which extends several hundred kilometers
516 behind the convective line, as seen in Johnson and Hamilton (1988).

517 A time dependent signal was found between the derecho strength and aerosol loading due
518 to the dynamics which produced the simulated derecho event. During the intensification stage of
519 MCS, the aerosol-induced changes in the precipitation formation, shown in Part I, impacted the
520 balance between the horizontal vorticity generated by the cold pool and that of the low-level
521 environmental wind shear (Rotunno et al., 1988). In this study, this balance was found to be
522 sensitive to aerosol loading through their impact on cold pool strength, which in turn, modified
523 the predominant flow which produced the DS winds at the surface from a descending RIJ (in the
524 CLEAN simulation) to an UDD (in the 5xPOLLUTED simulation). In the latter case, the weaker
525 cold pool was associated with a more upright oriented convective updraft, and a stronger meso-γ
526 vortex. As the storm matured, the changes in aerosol concentrations impacted the derecho event
527 by altering the intensity the meso-γ vortex and a non-monotonic trend with increase in aerosol
528 concentrations was observed, where the derecho event weakened only within the moderately
529 polluted simulation. Based on previous research, it is hypothesized here that these changes in the
530 cold pool affected the strength of the moeso-γ vortex by altering the amount of baroclinically-

generated horizontal vorticity which was made available to be tilted into the vertical (e.g van den Heever and Cotton 2004) and the fraction of horizontal vorticity tilted into the vertical (Atkins and St. Laurent, 2013). To confirm this, a vorticity budget analysis should be conducted as part of future work. Besides impacting the amount of horizontal relative vorticity which is made available to be tilted into the vertical (e.g van den Heever and Cotton 2004), a meso-γ vortex can be intensified by the generation of vertical relative vorticity due to stretching within a rotating updraft which is a function of the updraft speeds (Atkins and St. Laurent, 2009a). Since changes in aerosol number concentrations affect the redistribution of latent heat within the storm and subsequently the updraft speeds (Andreae et al., 2004; Khain et al., 2005; Koren et al., 2005; van den Heever et al., 2006; Li et al., 2008; Rosenfeld et al., 2008; Storer et al., 2010; Tao et al., 2012; Storer and van den Heever, 2013), these changes could be expected to impact meso-γ vortex intensity. Indeed, in this study, it was found that changes in aerosol concentration did impact updraft speeds (Fig. 19, Part I) and the meso-γ vortex intensity.

6. Conclusions

The microphysical effects of increased aerosol concentrations on the characteristics and intensity of a derecho were examined in this study by performing a numerical analysis of an MCS case study using a mesoscale cloud resolving model, RAMS. The case study chosen was the 8 May 2009 "Super-derecho" MCS. A set of three RAMS sensitivity simulations was conducted in which the aerosol distribution, number concentration and chemical composition differed based on the output of a 3D chemical model, GEOS-Chem. The CLEAN simulation contained only aerosol concentrations from non-anthropogenic sources, the POLLUTED included aerosols from both anthropogenic and non-anthropogenic sources and the

553 5xPOLLUTED had the same distribution as in the POLLUTED simulation, but multiplied by a
554 factor of five. Back trajectory analysis from grid points with derecho-strength winds were
555 performed for two periods within the storm: the intensification and dissipation stages. Analysis
556 of the sensitivity of the simulated derecho event to changes in aerosol concentration shows the
557 following:

558 • Changes in aerosol concentrations did not significantly impact the MCS longevity, total
559 precipitation or the formation of the derecho, however it did impact the distribution of
560 convective vs. stratiform precipitation (Part I) and the derecho characteristics (intensity
561 and area).
562 • Two air flows were found to produce the derecho event: a rear inflow jet (RIJ) and an up-
563 down downdraft (UDD) associated with a meso-γ vortex at the gust front.
564 • Aerosols acting as CCN were found to impact the derecho intensity directly by modifying
565 the cold pool strength and downdraft speeds, and indirectly by altering the balance
566 between the horizontal vorticity generated by the cold pool and that of the environment,
567 as well as the characteristics of the meso-γ vortex at the gust front.
568 • During the MCSs' intensification stage, an increase in aerosol concentration resulted in a
569 shift in the flow regime from being dominated by the RIJ to that of a downburst
570 following the pathway of an up-down downdraft, which exhibited stronger surface winds
571 speeds over a smaller area.
572 • During the MCSs' dissipation stage, the changes in the derecho characteristics were
573 attributed to the up-down downdraft associated with the meso-γ vortex in all three
574 simulations. At this time, acceleration within the up-down downdraft in the highly
575 polluted simulation was attributed to enhanced horizontal acceleration at higher altitudes

as the flow approached the stronger meso-γ vortex. Within the cleaner simulation, the flow was accelerated near the surface due to higher evaporation rates of hydrometeors. The meso-γ vortex at this time was the weakest within the moderately polluted simulation and did not produce an up-down downdraft which could contribute to derecho-strength winds at the surface.

The findings of this study are limited to the environment of this case study which included a strong and deep LLJ (Conigio et al., 2011) and anomalously high PW values which supported enhanced convective precipitation with increased aerosol concentration. The non-monotonic trends in the derecho characteristics with increased aerosol concentrations found in this study should be examined for other case studies with varying humidity.

Acknowledgements. The authors wish to thank Dr. Jeffery Pierce for providing the GOES-Chem aerosol data used in this study and Stephen Saleeby for his suggestions and input in simulating the 8 May 2009 case study MCS. This work was funded by the National Science Foundation under grant AGS-1005041.

7. References

1. Adams-Selin, R.D., van den Heever, S.C., Johnson, R.H., 2013. Impact of Graupel Parameterization Schemes on Idealized Bow Echo Simulations. Mon. Weather Rev. 141, 1241–1262.
2. Andreae, M.O., Rosenfeld, D., Artaxo, P., Costa, a a, Frank, G.P., Longo, K.M., Silva-Dias, M. a F., 2004. Smoking rain clouds over the Amazon. Science 303, 1337–1342.
3. Atkins, N.T., St. Laurent, M., 2009a. Bow Echo Mesovortices. Part II: Their Genesis. Mon. Weather Rev. 137, 1514–1532.
4. Atkins, N.T., St. Laurent, M., 2009b. Bow Echo Mesovortices. Part I: Processes That Influence Their Damaging Potential. Mon. Weather Rev. 137, 1497–1513.
5. Bernardet, L.R., Cotton, W.R., 1998. Multiscale Evolution of a Derecho-Producing Mesoscale Convective System. Mon. Weather Rev. 126, 2991–3015.
6. Bey, I., Jacob, D.J., Yantosca, R.M., Logan, J. a., Field, B.D., Fiore, A.M., Li, Q.-B., Liu, H.-Y., Mickley, L.J., Schultz, M.G., 2001. Global Modeling of Tropospheric Chemistry with Assimilated Meteorology: Model Description and Evaluation. J. Geophys. Res. 106, 73–95.
7. Bryan, G.H., Morrison, H., 2012. Sensitivity of a Simulated Squall Line to Horizontal Resolution and Parameterization of Microphysics. Mon. Weather Rev. 140, 202–225.
8. Charba, J., 1974. Application of Gravity Current Model to Analysis of Squall-Line Gust Front. Mon. Weather Rev. 102(2), pp.140-156.
9. Coniglio, M.C., Corfidi, S.F., Kain, J.S., 2012. Views on Applying RKW Theory: An Illustration Using the 8 May 2009 Derecho-Producing Convective System. Mon. Weather Rev. 140, 1023–1043.

620 10. Coniglio, M.C., Corfidi, S.F., Kain, J.S., 2011. Environment and Early Evolution of the 8
621 May 2009 Derecho-Producing Convective System. Mon. Weather Rev. 139, 1083–1102.
622 11. Cotton, W.R., Pielke Sr., R. a., Walko, R.L., Liston, G.E., Tremback, C.J., Jiang, H.,
623 McAnelly, R.L., Harrington, J.Y., Nicholls, M.E., Carrio, G.G., McFadden, J.P., 2003.
624 RAMS 2001: Current status and future directions. Meteorol. Atmos. Phys. 82, 5–29.
625 12. Emanuel, K.A., 1994. Atmospheric Convection. Oxford University.
626 13. Evans, C., Weisman, M.L., Bosart, L.F., 2014. Development of an Intense, Warm-Core
627 Mesoscale Vortex Associated with the 8 May 2009 “Super Derecho” Convective Event*.
628 J. Atmos. Sci. 71, 1218–1240.
629 14. Fan, J., Leung, L.R., Rosenfeld, D., Chen, Q., Li, Z., Zhang, J., Yan, H., 2013.
630 Microphysical effects determine macrophysical response for aerosol impacts on deep
631 convective clouds. Proc. Natl. Acad. Sci. U. S. A. 110, E4581-90.
632 15. Fujita, T.T., 1978. Manual of downburst identi_cation for project NIMROD. Technical
633 report, Dept. of Geophysical Sciences, University of Chicago, Chicago, IL.
634 16. Fujita, T.T., Wakimoto, R.M., 1981. Five Scales of Airflow Associated with a Series of
635 Downbursts on 16 July 1980. Mon. Weather Rev. 109, 1438–1456.
636 17. Grant, L.D., van den Heever, S.C., 2015. Cold Pool and Precipitation Responses to
637 Aerosol Loading: Modulation by Dry Layers. J. Atmos. Sci. 72, 1398–1408.
638 18. Grasso, L.D., 1996. Numerical simulation of the May 15 and April 26, 1991 tornadic
639 thunderstorm. Ph.D. dissertation, Colorado State University, 151 pp. [Available from
640 Department of Atmospheric Science, Colorado State University, Fort Collins, CO
641 80523.].
642 19. Hinrichs, G., 1888. Am. Meterological J. 1, 306–317.

643 20. Houze, R. a., Biggerstaff, M.I., Rutledge, S. a., Smull, B.F., 1989. Interpretation of
644 Doppler Weather Radar Displays of Midlatitude Mesoscale Convective Systems. Bull.
645 Am. Meteorol. Soc.
646 21. Johns, R.H., 1982. A synoptic climatology of northwest flow severe weather outbreaks.
647 Part I: Nature and significance. Mon. Wea. Rev. 110, 1653–1663.
648 22. Johns, R.H., Hirt, W.D., 1987. Derechos: Widespread Convectively Induced Windstorms.
649 Weather Forecast. 2, 32–49.
650 23. Johnson, R.H., Hamilton, P.J., 1988. The Relationship of Surface Pressure Features to the
651 Precipitation and Airflow Structure of an Intense Midlatitude Squall Line. Mon. Weather
652 Rev. 116, 1444–1473.
653 24. Keene, K.M., Schumacher, R.S., 2013. The Bow and Arrow Mesoscale Convective
654 Structure. Mon. Weather Rev. 141, 1648–1672.
655 25. Khain, A., Rosenfeld, D., Pokrovsky, A., 2005. Aerosol impact on the dynamics and
656 microphysics of deep convective clouds. Q. J. R. Meteorol. Soc. 131, 2639–2663.
657 26. Klimowski, B.A., Hjelmfelt. M. R., Bunkers, M.J., 2004. Radar observations of the early
658 evolution of bow echoes. Weather Forecast. 19, 727–734.
659 27. Knupp, K.R., 1987. Downdrafts within High Plains Cumulonimbi. Part I: General
660 Kinematic Structure. J. Atmos. Sci. 44(6), pp.987-1008.
661 28. Lebo, Z.J., Morrison, H., 2014. Dynamical Effects of Aerosol Perturbations on Simulated
662 Idealized Squall Lines. Mon. Weather Rev. 142, 991–1009.
663 29. Lee, S.S., Donner, L.J., Phillips, V.T.J., Ming, Y., 2008. Examination of aerosol effects
664 on precipitation in deep convective clouds during the 1997 ARM summer experiment. Q.
665 J. R. Meteorol. Soc. 134, 1201–1220.

30. Li, G., Wang, Y., Lee, K.H., Diao, Y., Zhang, R., 2009. Impacts of aerosols on the development and precipitation of a mesoscale squall line. J. Geophys. Res. Atmos. 114, 1–18.

31. Newton, C.W., 1950. Structure and mechanism of the prefrontal squall line. . J. Meteorol, 7(3), pp. 210-222.

32. Orlanski, I., 1975. A rational subdivision of scales for atmospheric processes. Am. Meteorol. Soc. 56, 527–530.

33. Parker, M.D., Johnson, R.H., 2000. Organizational Modes of Midlatitude Mesoscale Convective Systems. Mon. Weather Rev. 128, 3413–3436.

34. Przybylinksi, R.W., Schaumann, J.S., Cramer, D.T., Atkins, N.T., 2010. The 08 May 2009 Missouri Derecho : Radar Analysis and Warning Implications over Parts of Southwest Missouri, in: 25th Conf. on Severe Local Storms, Denver, CO, Amer. Meteor. Soc., 3B.1.

35. Rosenfeld, D., Lohmann, U., Raga, G.B., O'Dowd, C.D., Kulmala, M., Fuzzi, S., Reissell, A., Andreae, M.O., 2008. Flood or drought: how do aerosols affect precipitation? Science 321, 1309–13.

36. Rotunno, R., Klemp, J.B., Weisman, M.L., 1988. A Theory for Strong, Long-Lived Squall Lines. J. Atmos. Sci. 45(3), pp.463-485.

37. Saleeby, S.M., Heever, S.C., Marinescu, P.J., Kreidenweis, S.M. and DeMott, P.J., 2016. Aerosol effects on the anvil characteristics of mesoscale convective systems. J. Geophys. Res. 121.

38. Saleeby, S.M., van den Heever, S.C., 2013. Developments in the CSU-RAMS Aerosol Model: Emissions, Nucleation, Regeneration, Deposition, and Radiation. J. Appl.

689 Meteorol. Climatol. 52, 2601–2622.
690 39. Schmidt, J.M., Cotton, W.R., 1989. A High Plains Squall Line Associated with Severe
691 Surface Winds. J. Atmos. Sci.46(3), pp.281-302.
692 40. Seigel, R.B., van den Heever, S.C., 2013. Squall-Line Intensification via Hydrometeor
693 Recirculation. J. Atmos. Sci. 70, 2012–2031.
694 41. Seigel, R.B., van den Heever, S.C., Saleeby, S.M., 2013. Mineral dust indirect effects and
695 cloud radiative feedbacks of a simulated idealized nocturnal squall line. Atmos. Chem.
696 Phys. 13, 4467–4485.
697 42. Smull, B.F., Houze, R.A., 1987. Rear Inflow in Squall Lines with Trailing Stratiform
698 Precipitation. Mon. Weather Rev. 115, 2869–2889.
699 43. Storer, R.L., van den Heever, S.C., 2013. Microphysical Processes Evident in Aerosol
700 Forcing of Tropical Deep Convective Clouds. J. Atmos. Sci. 70, 430–446.
701 44. Tao, W.-K., Li, X., Khain, A., Matsui, T., Lang, S., Simpson, J., 2007. Role of
702 atmospheric aerosol concentration on deep convective precipitation: Cloud-resolving
703 model simulations. J. Geophys. Res. 112.
704 45. Tompkins, A.M., 2001. Organization of Tropical Convection in Low Vertical Wind
705 Shears: The Role of Cold Pools. J. Atmos. Sci. 58, 1650–1672.
706 46. van den Heever, S.C., Cotton, W.R., 2007. Urban aerosol impacts on downwind
707 convective storms. J. Appl. Meteorol. Climatol. 46, 828–850
708 47. van den Heever, S.C., Cotton, W.R., 2004. The Impact of Hail Size on Simulated
709 Supercell Storms. J. Atmos. Sci. 61, 1596–1609.
710 48. Wakimoto, R.M., Murphey, H. V., Davis, C.A., Atkins, N.T., 2006. High Winds
711 Generated by Bow Echoes. Part II: The Relationship between the Mesovortices and

712 Damaging Straight-Line Winds. Mon. Weather Rev. 134, 2813–2829.
713 49. Weisman, M.L., 1993. The Genesis of Severe, Long-Lived Bow Echoes. J. Atmos. Sci.
714 50, 645–670.
715 50. Weisman, M.L., 1992. The Role of Convectively Generated Rear-Inflow Jets in the
716 Evolution of Long-Lived Mesoconvective Systems. J. Atmos. Sci. 49(19), pp.1826-1847.
717 51. Weisman, M.L., Evans, C., Bosart, L., 2013. The 8 May 2009 Superderecho: Analysis of
718 a Real-Time Explicit Convective Forecast. Weather Forecast. 28, 863–892.
719 52. Weisman, M.L., Trapp, R.J., 2003. Low-Level Mesovortices within Squall Lines and
720 Bow Echoes. Part I: Overview and Dependence on Environmental Shear. Mon. Weather
721 Rev. 131, 2804–2823.
722 53. Xu, X., Xue, M., Wang, Y., 2015a. Mesovortices within the 8 May 2009 Bow Echo over
723 the Central United States: Analyses of the Characteristics and Evolution Based on
724 Doppler Radar Observations and a High-Resolution Model Simulation. Mon. Weather
725 Rev. 143, 2266–2290.
726 54. Xu, X., Xue, M., Wang, Y., 2015b. The Genesis of Mesovortices within a Real-Data
727 Simulation of a Bow Echo System. J. Atmos. Sci. 72, 1963–1986.s

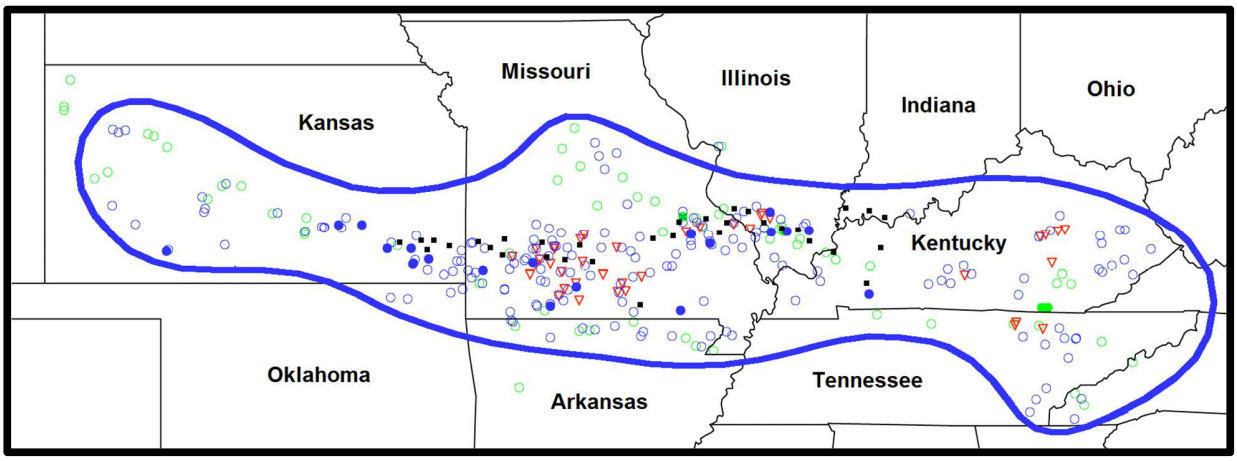

Figure 1: The area affected by the May 8, 2009 "Super Derecho" convective system and the severe weather reports associated with it (www.spc.noaa.gov). Area affected is outlined in blue. Severe reports are for the period from 0300-2300 UTC May 8, 2009. Wind damage or wind gusts ≥ 50 kts (58 mph) (open blue circles); estimated or measured wind gusts ≥ 65 kts (74 mph)(filled blue circles); hail ≥ 0.75 inches (open green circles); hail ≥ 2.0 inches (filled green circles); and tornados (red triangles) are all shown. Flash flooding (by county) is denoted by black squares. Area of most intense wind damage is approximated by band of filled blue circles extending from southeast Kansas through southern Missouri into southern Illinois.

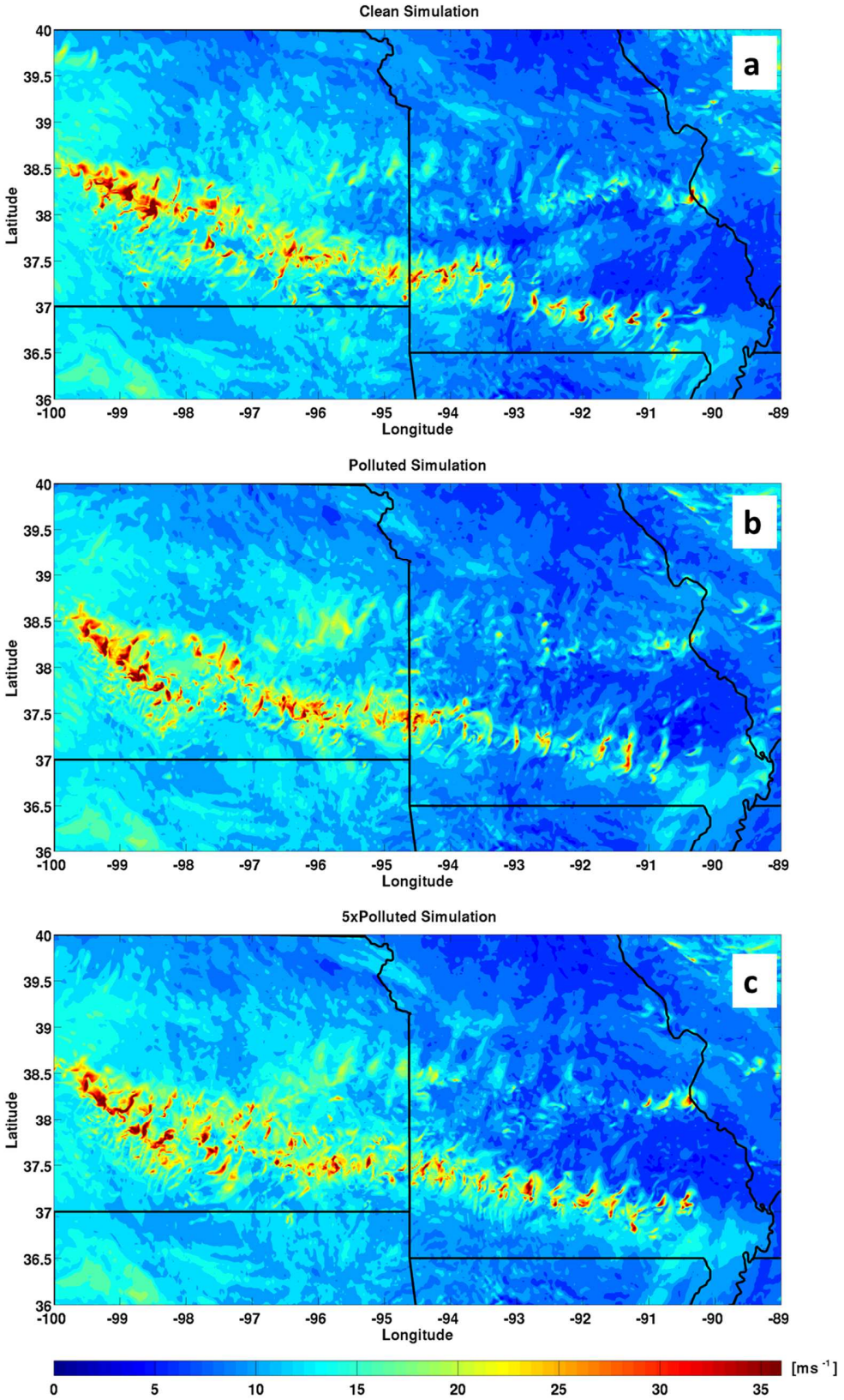

Fig. 2: Maximum surface wind speed [ms^{-1}] of the simulated MCS every 30 minutes during the analysis period (0630-1730 UTC) for the three simulations: (a) Clean, (b) Polluted and (c) 5xPolluted.

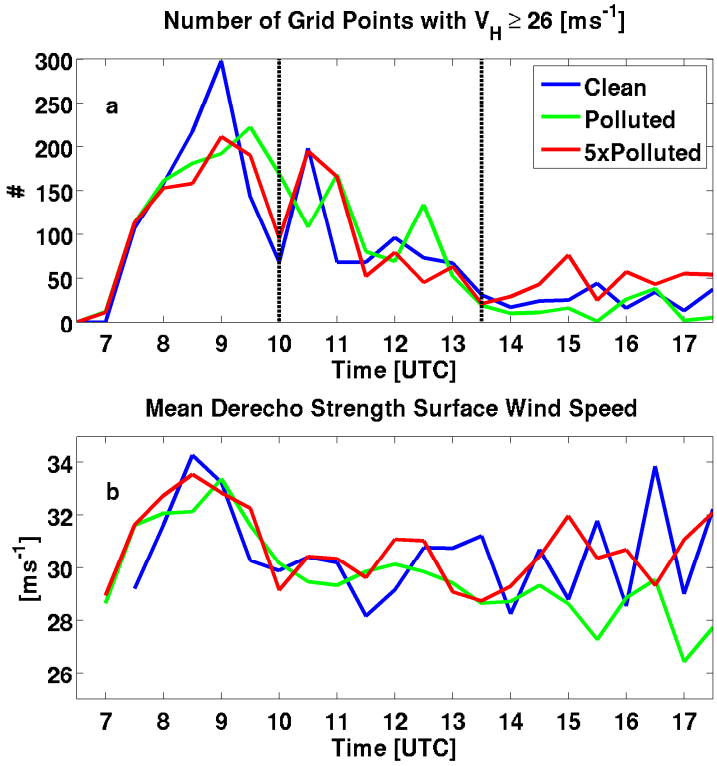

Fig. 3: Simulated (a) number of grid points with DS wind and (b) mean DS wind speed as a function of time for the Clean (blue), Polluted (green) and 5xPolluted (red) simulations. The dashed vertical lines, in 3a indicate the division of the MCS simulation in time to the three stages: intensification, mature and dissipation.

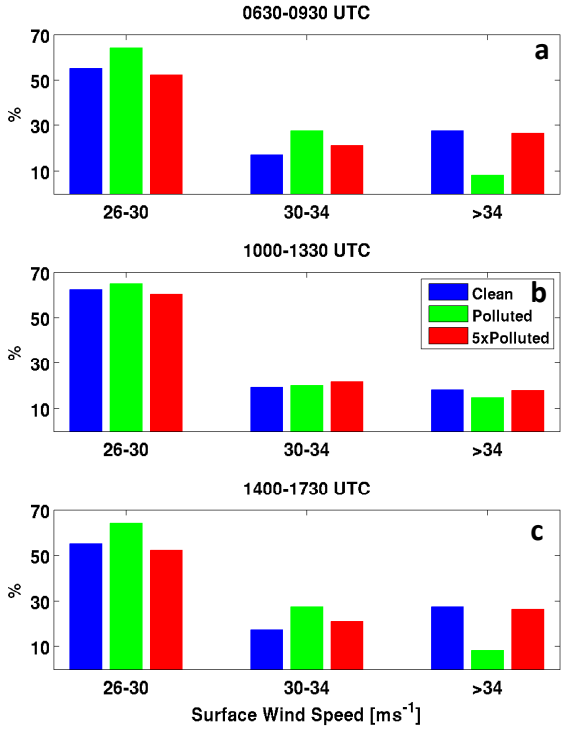

Fig. 4: Normalized distribution of DS wind speeds for the Clean (blue), Polluted (green), and 5xPolluted (red) simulations during (a) the intensification stage 0630-0930 UTC, (b) the mature stage 1000-1330 UTC, and (c) the dissipation stage 1400-1730 UTC.

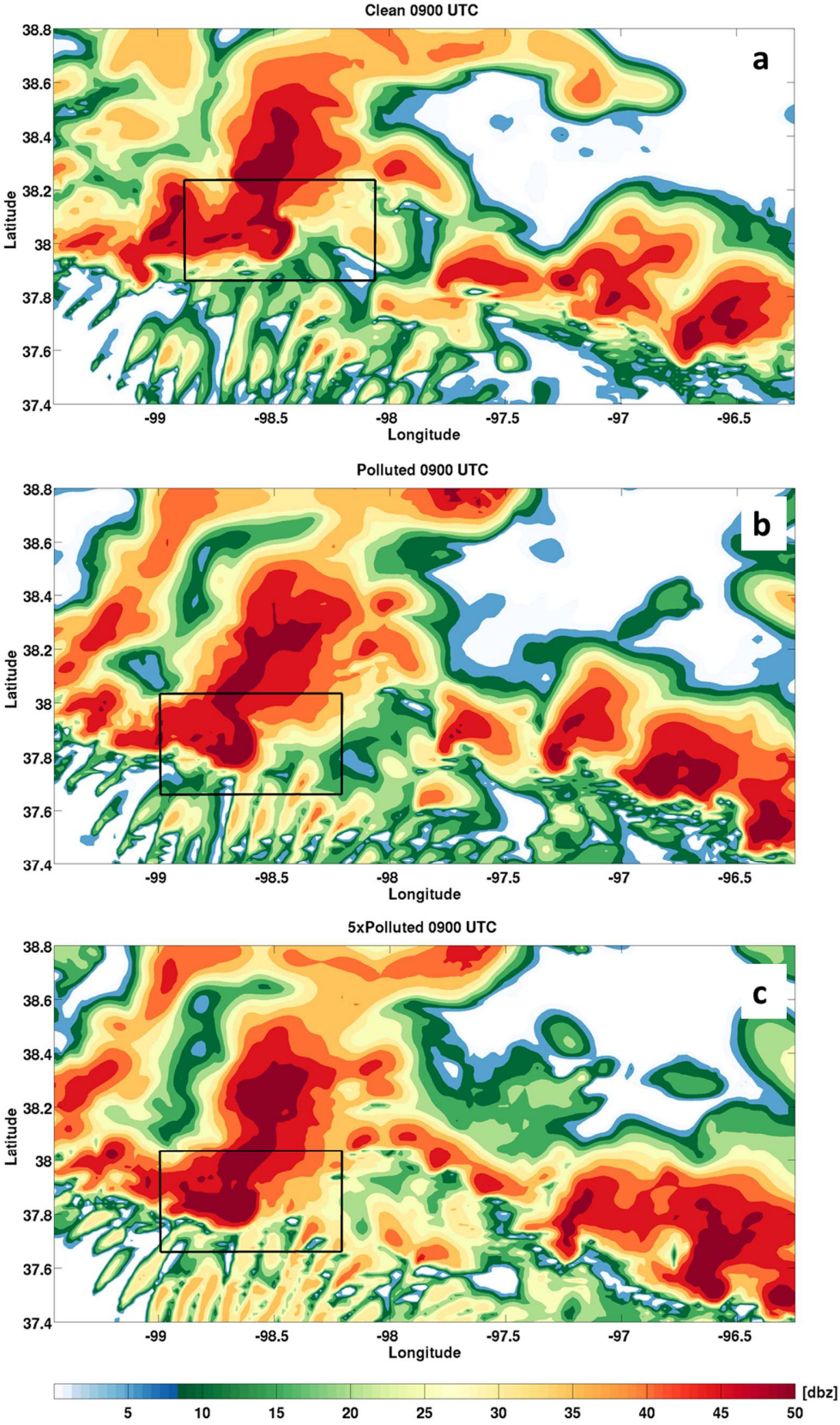

Fig. 5: Simulated radar reflectivity at 1km at 0900 UTC for the three simulations: Clean (a), Polluted (b) and 5xPolluted (c). The analyzed region is enclosed within a black rectangle.

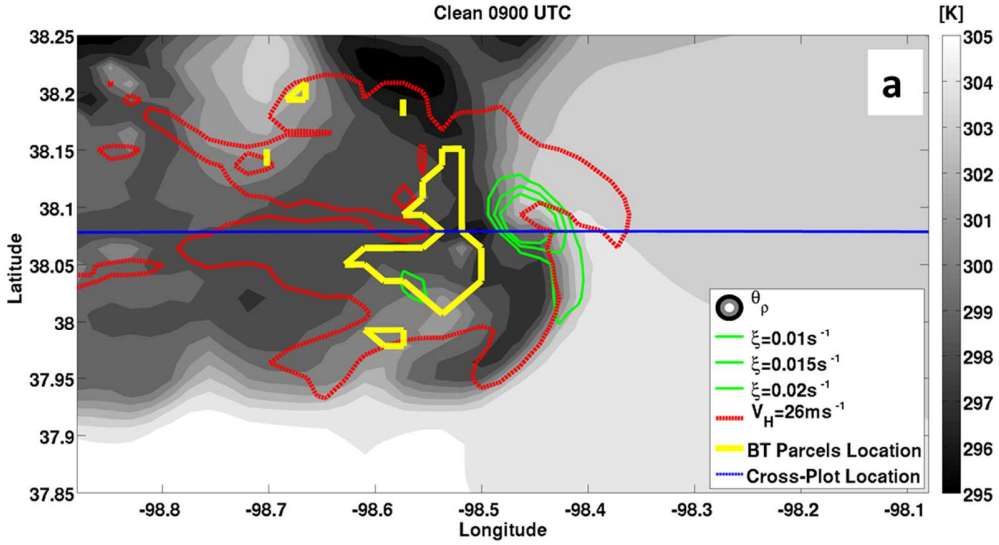
Clean 0900 UTC
[K]
a
Latitude
Longitude
θ_ρ
ξ=0.01s^{-1}
ξ=0.015s^{-1}
ξ=0.02s^{-1}
V_H=26ms^{-1}
BT Parcels Location
Cross-Plot Location

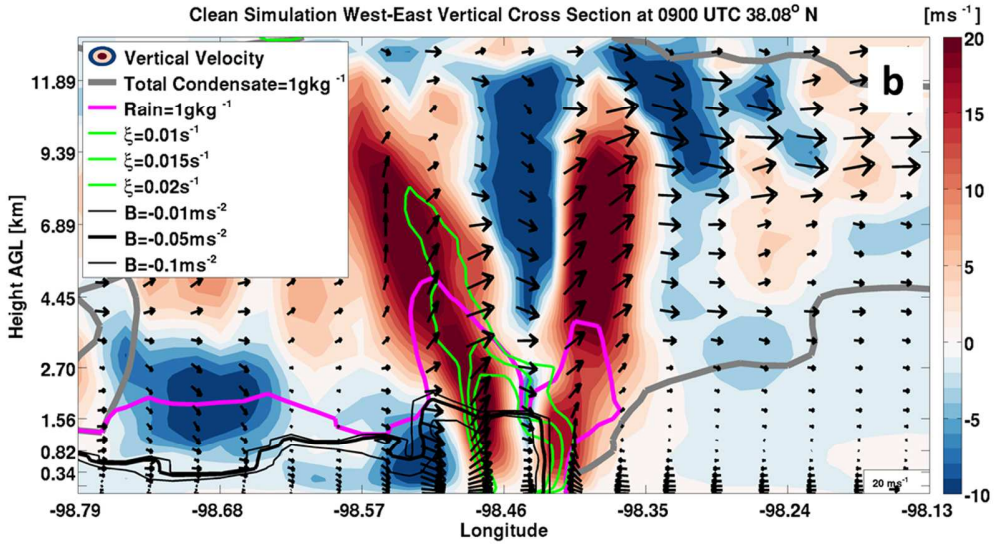
Clean Simulation West-East Vertical Cross Section at 0900 UTC 38.08° N
[ms^{-1}]
b
Height AGL [km]
Longitude
Vertical Velocity
Total Condensate=1gkg^{-1}
Rain=1gkg^{-1}
ξ=0.01s^{-1}
ξ=0.015s^{-1}
ξ=0.02s^{-1}
B=-0.01ms^{-2}
B=-0.05ms^{-2}
B=-0.1ms^{-2}
20 ms^{-1}

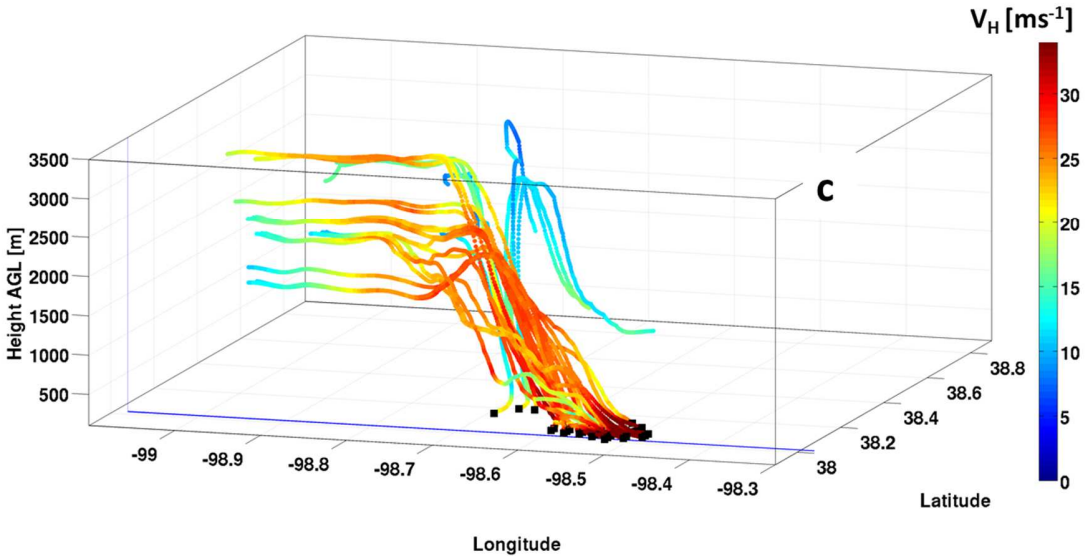
V_H [ms^{-1}]
c
Height AGL [m]
Longitude
Latitude

Fig. 6: Clean simulation at 0900 UTC: (a) Surface density potential temperature θρ [K] (shaded) of the area enclosed by the black rectangle in Figure 5a. Superimposed are contours of vertical relative vorticity at 1km AGL ($0.01s^{-1}$, $0.015s^{-1}$ and $0.02s^{-1}$ isopleths) representing the location of the meso-γ vortex at the gust front (green contours). The area with DS winds is contoured in red and the region with the location of the back trajectories analyzed contoured in yellow. Only back trajectories that descended above ground level were analyzed. The blue line across the figure presents the location of the cross plot within figure b. The location of this cross section was chosen along the mean location of the DS winds at the gust front. (b) Vertical cross section along the blue line shown in figure (a) of the vertical velocity [ms^{-1}] (shaded), with the (u,w) wind vectors and the meso-γ vortex represented in green contours of $0.01s^{-1}$, $0.015s^{-1}$ and $0.02s^{-1}$ relative vertical vorticity isopleths. The outline of the system is represented by the 1 gkg^{-1} contour of the total condensate (grey) and the precipitation by the 1 gkg^{-1} rain mixing ratio isopleth (magenta). The gust front is represented by the buoyancy value (B) of the cold pool contoured in black, as calculated according the density potential temperature. The edge of the cold pool is defined according to the isopleth of -0.05 ms^{-2}, a value representative of mid-latitude cold pools (Seigel et al. 2013). Additional buoyancy value of -0.01 m s^{-2} and -0.1 m s^{-2} are also plotted to show the cold pool magnitude. (c) 30 minute back trajectories (a sample size of 30) of the parcels within the region contoured in thicker red (figure a) and their relative location to the cross plot (figure b) (represented by the blue contour).The trajectories are colored according to the horizontal wind speed of the parcel along the trajectories. The vertical extent of the plot is 3500 meters AGL.

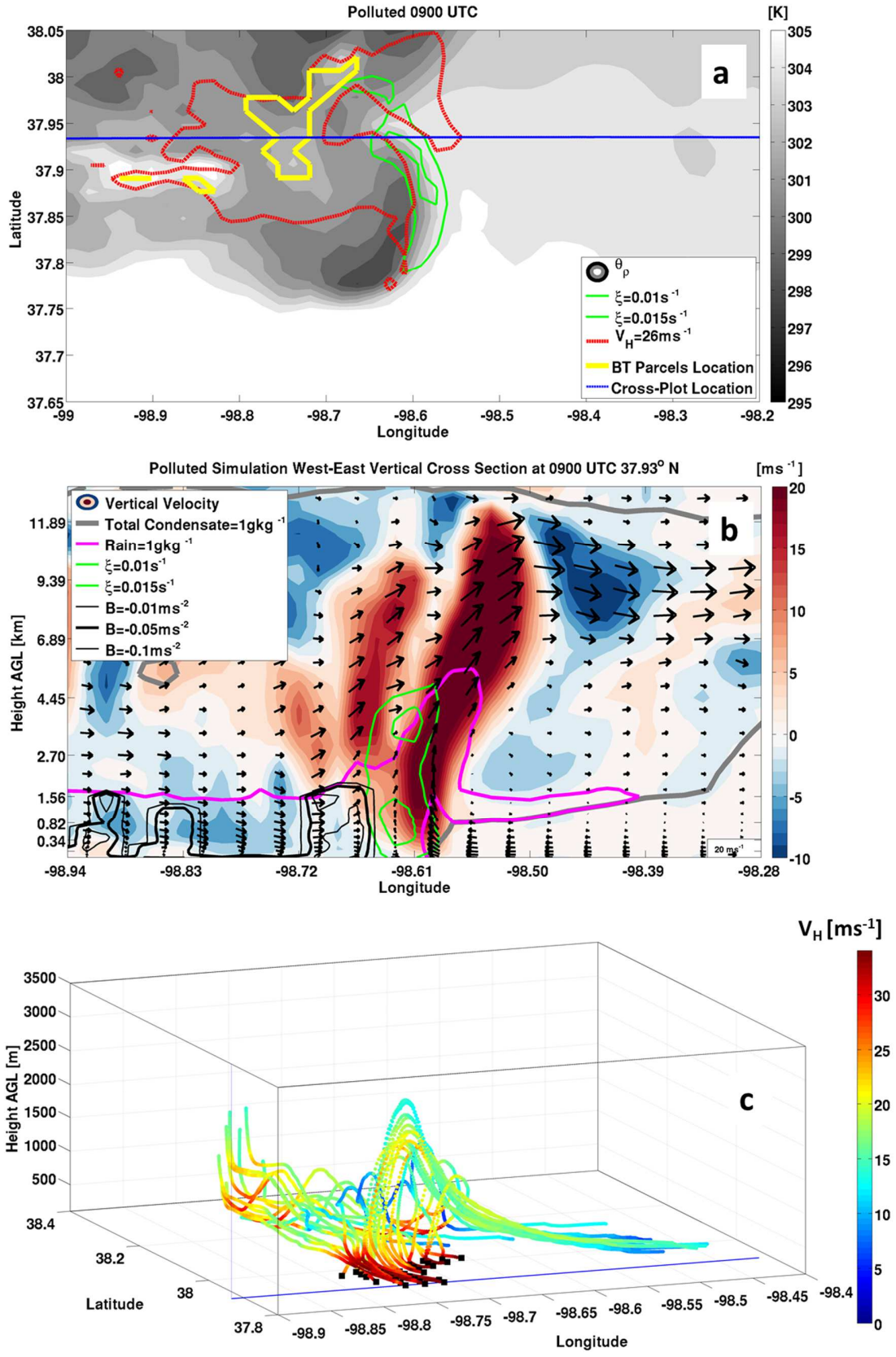

Fig. 7: Same as Fig. 6, for the Polluted simulation at 0900 UTC.

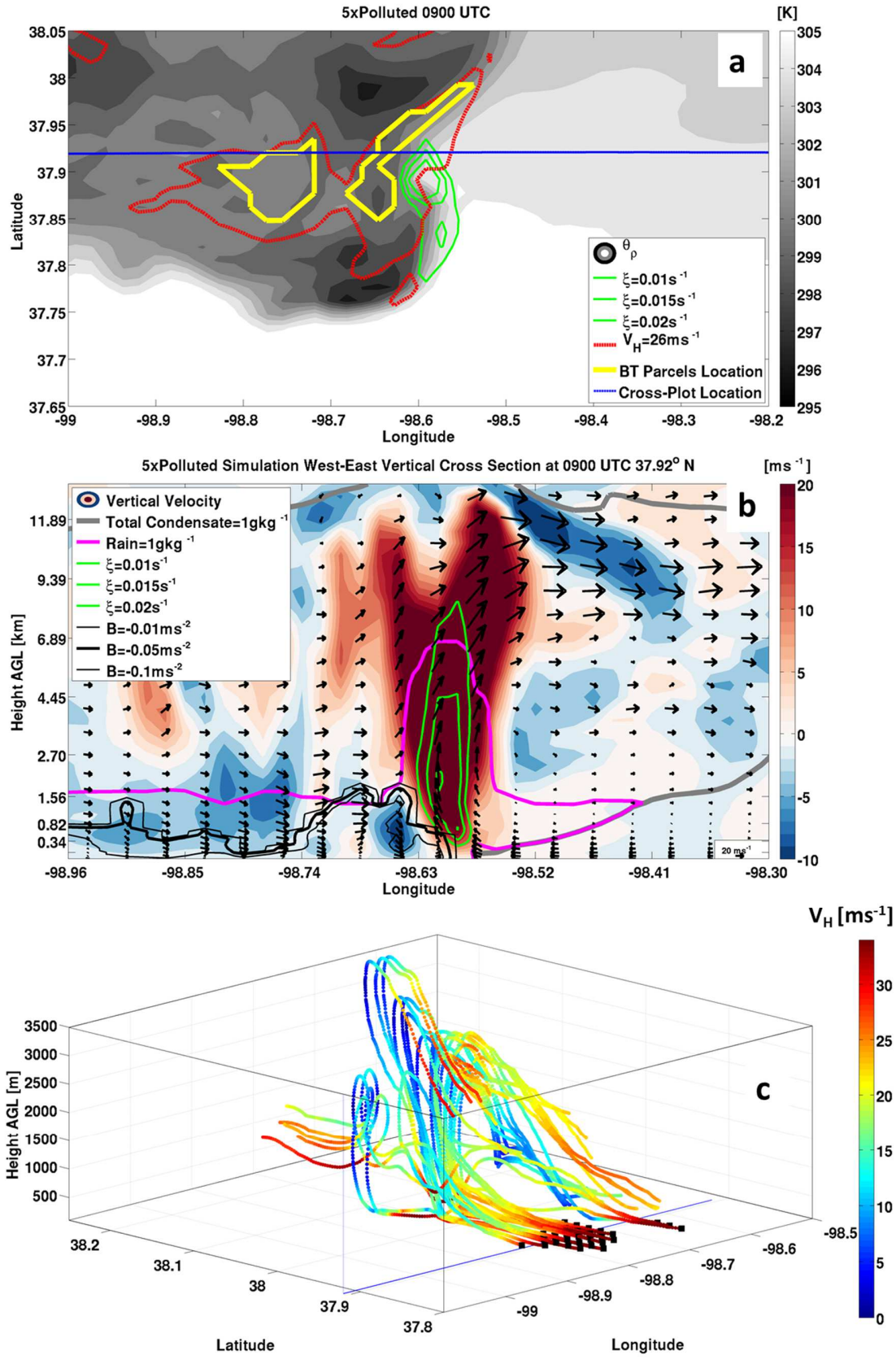

Fig. 8: Same as Fig. 6, for the 5xPolluted simulation at 0900 UTC.

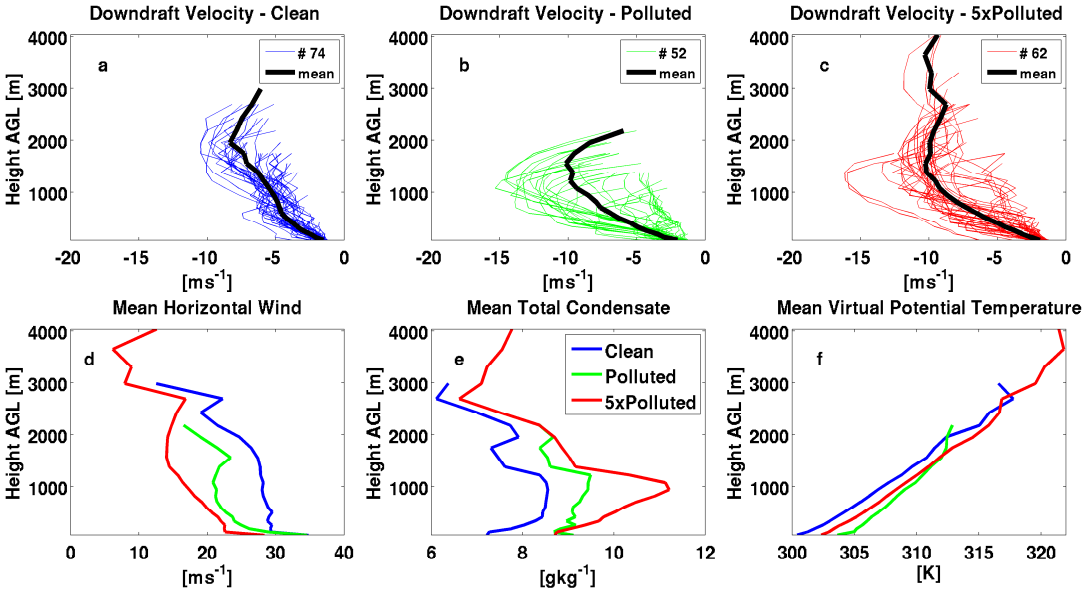

Figure 9: Downdraft vertical velocity as a function of height for individual descending parcels that follow either the RIJ or the UDD and the mean vertical velocity for the Clean (a), Polluted (b) and 5xPolluted (c) back trajectory analysis. The number in parenthesis represents the number of parcels. Mean characteristics of the descending parcels of horizontal wind speed [ms^{-1}] (d), condensate loading [gkg^{-1}] (e) and mean virtual potential temperature [K] (f) for the Clean (blue), Polluted (green) and 5xPolluted (red) simulations are plotted as a function of height for the downdraft trajectories.

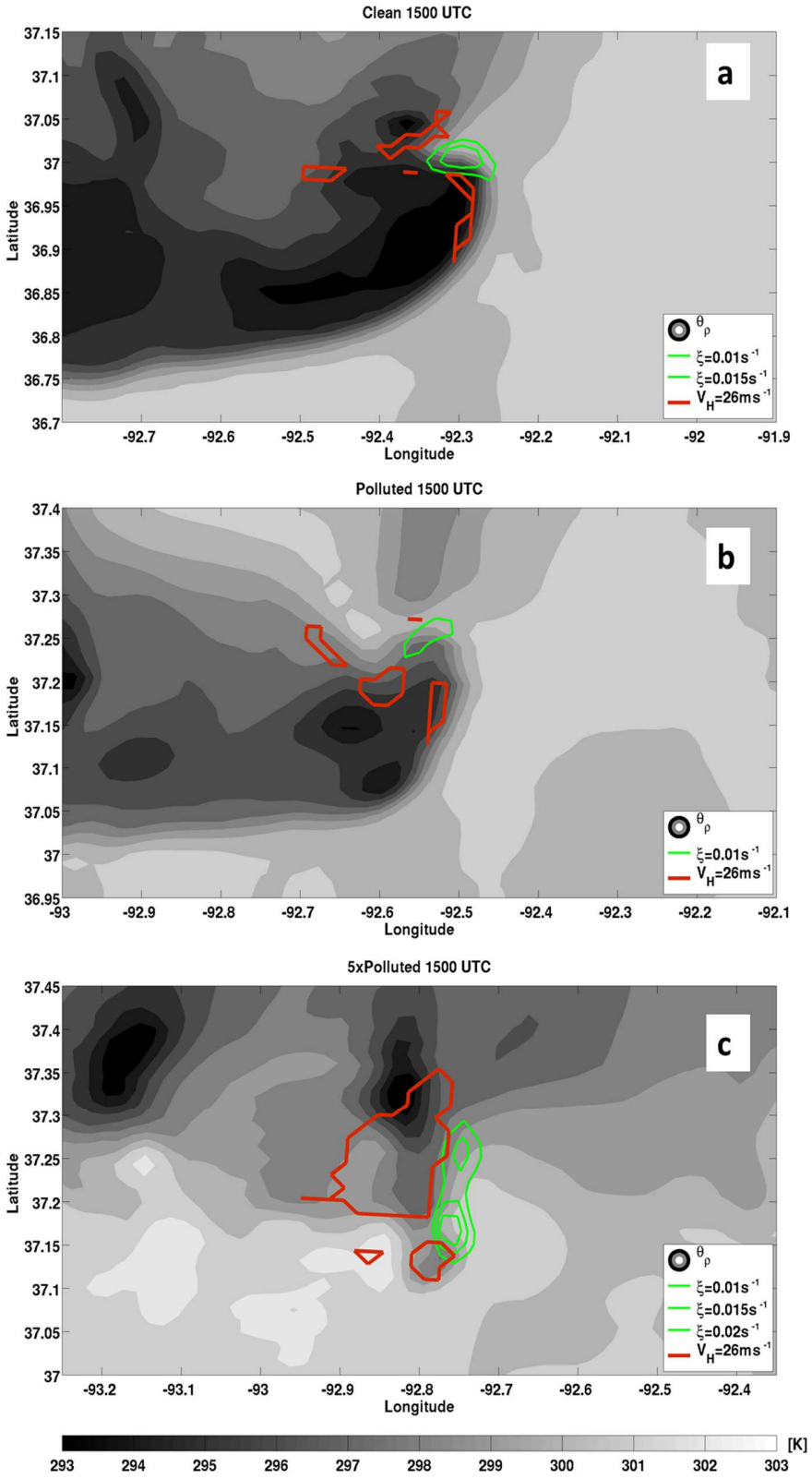

Figure 10: Surface density potential temperature (shaded), locations of DS winds (contoured in red) and the mesovortex at 1km AGL (contoured in green) are presented for the Clean (a), Polluted (b) and 5xPolluted (c) simulations at 1500 UTC.

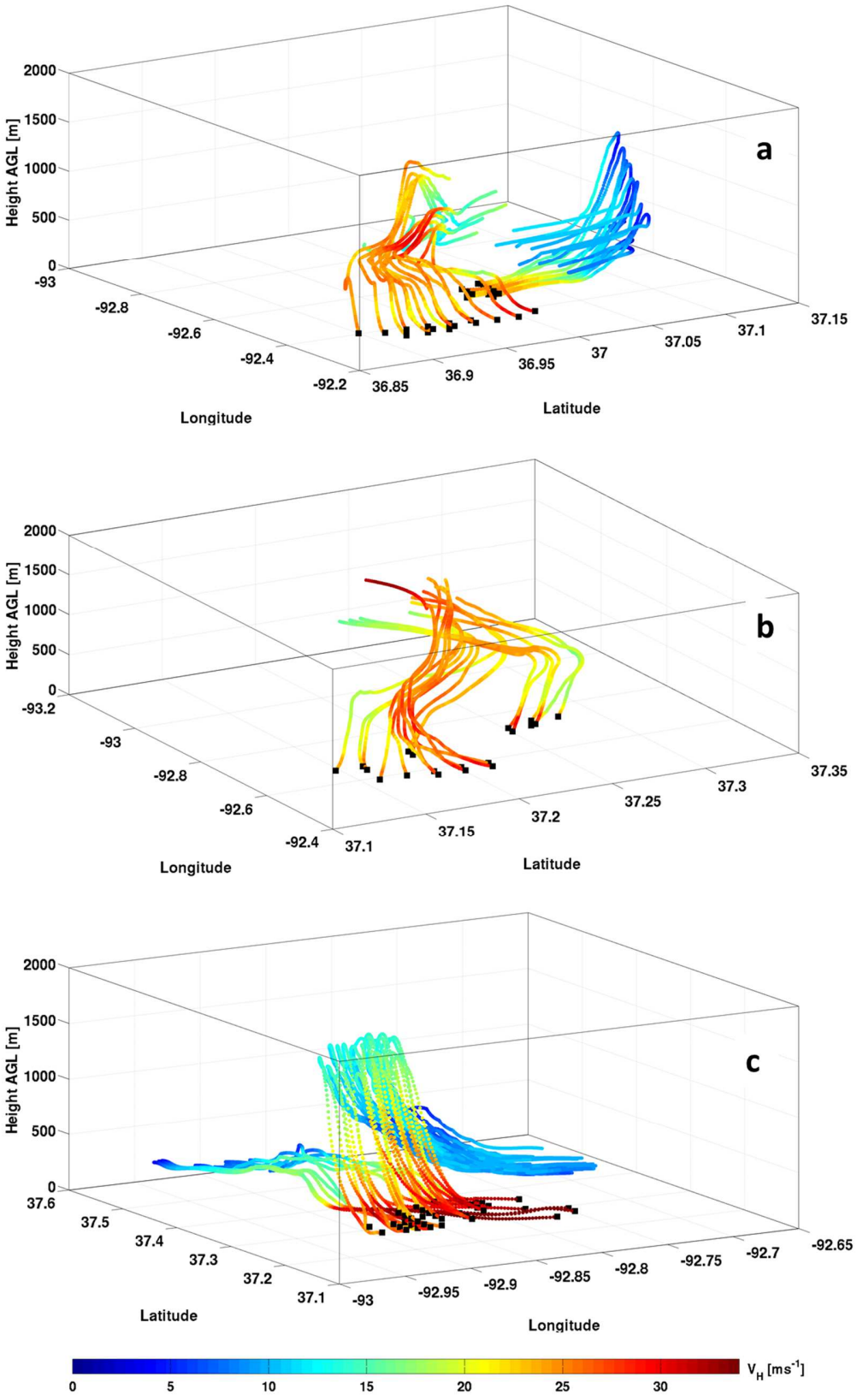

Fig. 11: 1500 UTC sample 3D back-trajectory plots during 30 minutes for the (a) Clean, (b) Polluted and (c), 5x Polluted simulations. Trajectories are colored according to the parcel's horizontal wind speeds. Origins of the back-trajectories (at 1500 UTC, near the surface) are noted by the black square marker.

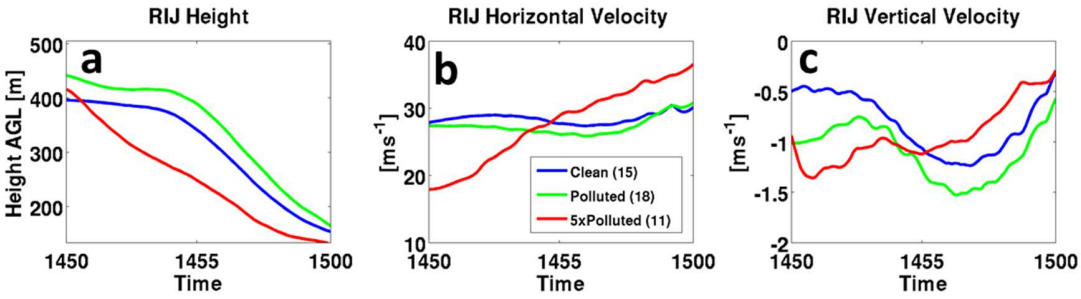

Fig. 12: 1500 UTC mean back trajectory parcel characteristics of (a) height, (b) horizontal velocity and (c) vertical velocity for the Clean (blue), Polluted (green) and 5xPolluted (red) simulations during the last 10 minutes of the parcels descent. Numbers in the brackets within the legend represent the number of parcels following the RIJ BT flow.

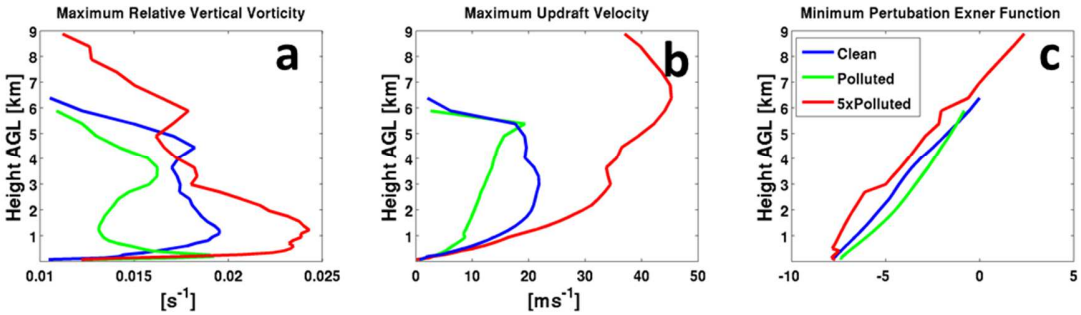

Fig. 13: Characteristics of the Mesovortex (within a region of relative vertical vorticity greater than 0.01 s^{-1}(a) maximum relative vertical vorticity, (b) maximum updraft velocity and the (c) minimum Exner perturbation function with height for the three simulations: Clean (blue), Polluted (green) and 5xPolluted (red).

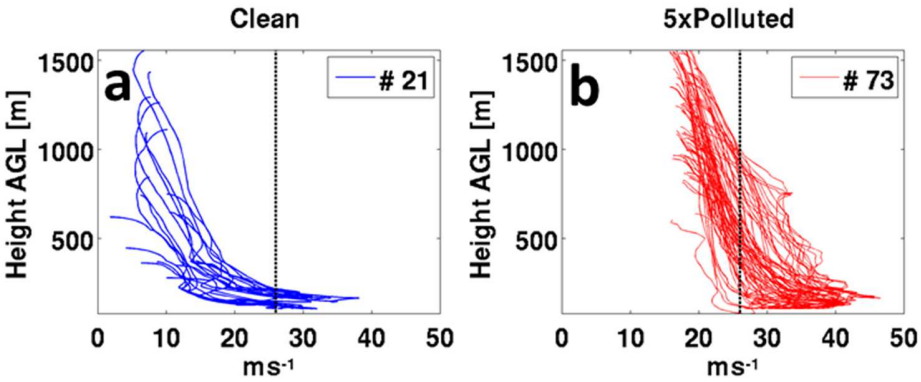

Fig. 14: Horizontal wind speed of parcels during the decent following the UDD for the Clean (left) and 5xPolluted simulations (right). Numbers in the legend represent the number of parcels plotted, determined by the region in figure 11a and 11c.

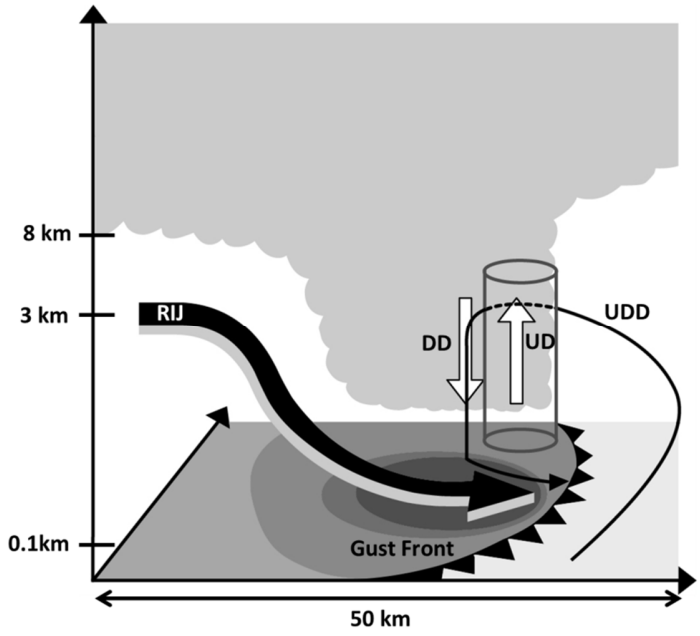

Fig. 15: Schematic depiction summarizing the 3D flow of the Rear-Inflow Jet (RIJ) and Up-down downdraft (UDD), the meso-γ vortex at the gust relative to the location of the cold pool (shaded in the X-Y plan) and gust front, the convective updraft (UD) and precipitating convective downdraft (DD).